A spatially continuous magnetization model for Mars

A spatially continuous magnetization model for Mars

K. A. Whaler
School of GeoSciences, University of Edinburgh, Edinburgh, UK

M. E. Purucker
Raytheon ITSS at Planetary Geodynamics Laboratory, NASA/GSFC, Greenbelt, Maryland, USA

Received 23 December 2004; revised 6 May 2005; accepted 19 May 2005; published 2 September 2005.

[1] Using a three-component magnetic field data set at over 100,000 satellite points previously compiled for spherical harmonic analysis, we have produced a continuously varying magnetization model for Mars. The magnetized layer was assumed to be 40 km thick, an average value based on previous studies of the topography and gravity field. The severe nonuniqueness in magnetization modeling is addressed by seeking the model with minimum root-mean-square (RMS) magnetization for a given fit to the data, with the trade-off between RMS magnetization and fit controlled by a damping parameter. Our preferred model has magnetization amplitudes up to 20 A/m. It is expressed as a linear combination of the Green's functions relating each observation to magnetization at the point of interest within the crust, leading to a linear system of equations of dimension the number of data points. Although this is impractically large for direct solution, most of the matrix elements relating data to model parameters are negligibly small. We therefore apply methods applicable to sparse systems, allowing us to preserve the resolution of the original data set. Thus we produce more detailed models than any previously published, although they share many similarities. We find that tectonism in the Valles Marineris region has a magnetic signature, and we show that volcanism south of the dichotomy boundary has both a magnetic and gravity signature. The method can also be used to downward continue magnetic data, and a comparison with other leveling techniques at Mars' surface is favorable.

Citation: Whaler, K. A., and M. E. Purucker (2005), A spatially continuous magnetization model for Mars, *J. Geophys. Res.*, *110*, E09001, doi:10.1029/2004JE002393.

1. Introduction

[2] The Mars Global Surveyor (MGS) mission has produced a step change in our knowledge of the magnetic field of Mars. Launched in 1996, its highest resolution was achieved during the aerobraking (AB) phase at distances of less than 100 km from the planet. The AB data provided the spectacular images of strongly magnetic, stripe-like features in the southern hemisphere [e.g., *Connerney et al.*, 1999].

[3] The details of the mission phases have been described in detail elsewhere [e.g., *Albee et al.*, 2001], so we summarize only their main features. After MGS was inserted into orbit around Mars in 1997, the AB phase brought the orbit from highly elliptical to almost circular. Due to a problem with the deployment of a solar panel, this phase was split into two, lasting 5 (AB1) and 7 (AB2) months, respectively, separated by the Science Phasing Orbit (SPO), a 6 month period during which the orbit drifted into its proper position with respect to the sun. The periapsis of the SPO orbit was as close as 80 km to the surface defined by a reference radius of 3393.5 km. The satellite has been in the Mapping Orbit (MO or MPO) phase, a near circular orbit at about 400 km above the surface, since 1999.

0148-0227/05/2004JE002393

[4] With the Martian dynamo thought to have operated for only the first half a billion years or so of the planet's history [e.g., *Acuña et al.*, 2001], the largest contribution to the observed field comes from its permanently magnetized crust, the focus of this study. However, there are uncertainties in its determination due to a number of factors. These include magnetometer drift, spacecraft fields, external fields and unmodeled fields. The absence of secular variation [*Purucker et al.*, 2003] suggests that magnetometer drift is minimal. The magnetic instrumentation on board MGS consists of two, solar-panel mounted triaxial fluxgate magnetometers, allowing spacecraft-generated fields to be estimated. Both preflight and inflight calibration has taken place, resulting in the removal of both static and dynamic spacecraft fields [*Acuña et al.*, 2001]. The two main sources of external fields are mini-magnetospheres in the south, and fields entering and leaving the ionopause at altitudes of approximately 400 km, depending on the internal field strength. As external fields are maximum in the day-time, we use only night-time MO data, but data acquired at all local times during the aerobraking phases. This is due both to the scarcity of AB data (these phases of the mission lasted only 12 months in total), and because the AB phase brought MGS closest to the Martian surface, providing the best resolution of the magnetic field. External fields are thought

to affect preferentially the horizontal components of the internal field [*Acuña et al.*, 2001], which is why preliminary studies [e.g., *Purucker et al.*, 2000] concentrated on modeling the radial field component data. Unmodeled fields, including toroidal fields, are a further source of uncertainty.

[5] Most previous work has concentrated on either spherical harmonic or equivalent dipole models of the crustal field, and their interpretation. Equivalent dipole models have long been used to model the terrestrial crustal magnetic field, both from satellite and aeromagnetic data [e.g., *Ravat et al.*, 2002]. In the terrestrial case, a significant proportion of the crustal field is due to induced magnetization, so that the equivalent dipoles can be assumed to be aligned with the Earth's main magnetic field. In the absence of a main field on Mars, the dipole directions are unknown, and should be solved for alongside the magnetization strength. Earlier studies instead made arbitrary assumptions as to the dipole directions. For instance, *Purucker et al.* [2000] produced a discrete, global magnetization model utilizing only radial component data, arranging radially directed equivalent dipoles on a spherical icosahedral tessellation with 110 km average spacing. However, *Langlais et al.* [2004] produced a discrete, global magnetization model from a three-component data set with arbitrary dipole directions. Due to the nonlinearities introduced by solving for directions as well as magnitudes, which greatly increases the computational effort, they limited their dipole spacing to an average of 173 km, again on a spherical icosahedral tessellation. *Arkani-Hamed* [2002a] inverted for vertically integrated crustal magnetization (in a 50 km thick layer), expressed through spherical harmonic coefficients, assuming it was caused by a dipole field with paleopole position determined from forward modeling of isolated magnetic anomalies. Spherical harmonic analysis results include the degree and order 50 and 90 models of *Arkani-Hamed* [2002b, 2004] and *Cain et al.* [2003], utilizing all three field components, and data from a range of altitudes. *Parker* [2003] used ideal body theory to put analytical bounds on magnetization strength for the Martian crustal field.

[6] Here we derive and present a three-component magnetization model from three-component data at a range of altitudes and local times. We model magnetization as a linear combination of the Green's functions relating magnetization at any point in the magnetized crust to a satellite measurement of the magnetic field. This avoids subjective choices of the arrangement of equivalent dipoles, and produces a spatially continuous magnetization model preserving the resolution of the original data set. More details are given in section 2. Our primary objective is to produce a model suitable for tectonic and structural interpretation, but it can also be used to predict the field at any position above the Martian surface, thereby providing a means of leveling (upward and downward continuing) data measured at a number of different altitudes. Due to the disparate data types, we must weight the data appropriately; this is discussed in section 3.

[7] *Runcorn* [1975] demonstrated that the form of the nonuniqueness for the magnetization inversion problem is particularly severe. Here, we find the unique solution minimizing root-mean-square (RMS) magnetization subject to a given fit to the data. An infinity of other solutions exist satisfying the data equally well, but must have higher magnetizations. This is an example of minimum norm modeling, a strategy commonly employed in geophysical inversion [*Parker*, 1994]. The norm minimized is often a measure of spatial smoothness, following the Occam's razor philosophy; here we minimize the quantity of interest itself rather than its gradient. Damped least squares methods, amongst the most widely employed inversion techniques, for equivalent dipole sources also minimize RMS magnetization amplitude [*Whaler and Langel*, 1996]. Backus-like ambiguities [*Maus and Haak*, 2003] do not affect Mars because it has no main field. By using satellite measurements of the field at altitudes several times the thickness of the magnetized crust, we have no resolution of the depth variation of magnetization. However, vertically integrated magnetization is well resolved.

2. Method

[8] We base our methodology for producing a continuously spatially varying magnetization model on the integral relation between the magnetization vector and an observation of a field component on or above the Martian surface [*Parker et al.*, 1987; *Jackson*, 1990; *Whaler and Langel*, 1996]. Let $\mathbf{M}(\mathbf{s})$ be magnetization at any point $\mathbf{s}$ within the Martian magnetized crust, and let $B^{(\eta)}(\mathbf{r}_j)$ be a satellite altitude measurement of the η component of the magnetic field. Then

$$B^{(\eta)}(\mathbf{r}_j) = -\hat{\mathbf{l}}_j^{(\eta)} \cdot \nabla_{\mathbf{r}_j} \int_V \mathbf{H}(\mathbf{r}_j, \mathbf{s}) \cdot \mathbf{M}(\mathbf{s}) dV \tag{1}$$

$$\equiv \int_V \mathbf{G}^{(\eta)}(\mathbf{r}_j, \mathbf{s}) \cdot \mathbf{M}(\mathbf{s}) dV \tag{2}$$

where the subscript on the ∇ operator indicates whether derivatives are with respect to satellite datum coordinates or those denoting position within the magnetized crust, V is the volume of the magnetized crust, and $\hat{\mathbf{l}}_j^{(\eta)}$ is the unit vector in the direction of the appropriate orthogonal field component, i.e., r, θ, or ϕ, working in spherical polar coordinates. $\mathbf{H}(\mathbf{r}_j, \mathbf{s}) = \frac{\mu_0}{4\pi} \nabla_s \frac{1}{|\mathbf{r}_j - \mathbf{s}|}$ is the Green's function relating magnetization to magnetostatic potential.

[9] Due to the inherent nonuniqueness, we seek the best-fitting magnetization model minimizing the norm

$$\int_V \mathbf{M}^2 dV \tag{3}$$

i.e., we minimize the RMS magnetization within the magnetized crust, for which the solution is [*Shure et al.*, 1982; *Parker*, 1994]

$$(\mathbf{\Gamma} + \lambda \mathbf{I})\boldsymbol{\alpha} = \mathbf{d} \tag{4}$$

where $\mathbf{d}$ is the data vector, $\boldsymbol{\alpha}$ the solution vector, and λ a damping parameter controlling the relative importance of fit to the data and the RMS magnetization. The Gram matrix, $\mathbf{\Gamma}$, is [*Parker et al.*, 1987; *Jackson*, 1990; *Whaler and Langel*, 1996]

$$\Gamma_{ij}^{(\eta\nu)} = \int_V \mathbf{G}^{(\eta)}(\mathbf{r}_i, \mathbf{s}) \cdot \mathbf{G}^{(\nu)}(\mathbf{r}_j, \mathbf{s}) dV \tag{5}$$

Then [*Parker et al.*, 1987]

$$\mathbf{M}(\mathbf{r}) = \sum_{j=1}^{N} \alpha_j^{(\eta)} \mathbf{G}^{(\eta)}(\mathbf{r}, \mathbf{r}_j) \tag{6}$$

where N is the number of data, and the superscript on components of $\boldsymbol{\alpha}$ indicates which component the jth datum measured. The functional form of $\mathbf{G}$ means that the magnetization solution calculated from (6) decreases with depth in the magnetized layer.

[10] For a typical satellite data set of several hundred thousand points, it is impractical to solve (4) directly. Previously, *Whaler and Langel* [1996] used a so-called depleted basis [*Parker and Shure*, 1982], expressing the magnetization through (6) at only a subset of the data points. The problem then reduces to solving a linear system of dimension the number of depleted basis points. However, the choice of depleted basis is subjective, and reduces the resolution of the model to the spacing between the basis points.

[11] To preserve the resolution of the data but create a tractable computational problem, we take advantage of the numerical sparseness of the Gram matrix (5). The functions $\mathbf{G}^{(\eta)}$ as a function of angular separation (subtended at the centre of Mars) between the observation point $\mathbf{r}_j$ and a point $\mathbf{s}$ within the magnetized crust are strongly peaked around zero, with a width of a few degrees (for observations at a typical MGS altitude above the Martian surface). Thus their product, the integrand of the expressions for the Gram matrix elements in (5), is vanishingly small, and hence so is the resulting integral, unless the observation points i and j are within a few degrees of each other. We can therefore use algorithms for solving sparse matrix systems; following *Purucker et al.* [1996], we chose to apply the iterative conjugate gradient (CG) method with compressed row storage to solve (4). If the absolute value of a matrix element was below a specified threshold, then it was treated as if it was zero. The threshold value was determined by the memory available on the computer system we used.

[12] Preconditioning can improve considerably the convergence of iterative algorithms such as CG. We used Jacobi scaling, whereby each matrix element $\Gamma_{ij} + \lambda\delta_{ij}$ of (4) is divided by $\sqrt{[(\Gamma_{ii} + \lambda)(\Gamma_{jj} + \lambda)]}$, such that the diagonal elements are all unity. Each datum d_i is divided by $\sqrt{(\Gamma_{ii} + \lambda)}$, and consequently we solve for the vector $\{\alpha_j\sqrt{(\Gamma_{jj} + \lambda)}, j = 1, \ldots, N\}$, and remove the preconditioning factor subsequently. Thus the rapidity with which the CG algorithm converges is also governed by the size of the damping parameter, λ.

[13] The majority of the computational effort goes into calculating the Gram matrix elements, even though they have closed form expressions [*Jackson*, 1990; *Whaler and Langel*, 1996] when the magnetized layer is assumed to be of uniform thickness. Fortunately, FORTRAN90 code to evaluate the matrix parallelizes efficiently using OpenMP; we actually parallelized the whole program to solve for $\boldsymbol{\alpha}$ (and calculate numbers characterizing the solution, such as the misfit and RMS magnetization) in OpenMP, including the CG algorithm. Here, we specified a thickness of 40 km, an average of the estimates north and south of the dichotomy of *Zuber et al.* [2000], *Lemoine et al.* [2001], *Smith et al.* [2001], *Nimmo and Gilmore* [2001], and *Neumann et al.* [2004]. Since this is much smaller than the radius of the planet, we can use the approximate expressions given by *Whaler and Langel* [1996, Appendix B]. Calculations from terrestrial data have shown that the effect of varying the thickness of the magnetized layer is to vary the RMS magnetization such that the vertically integrated magnetization is constant, without altering the magnetization pattern.

3. Data

[14] We used the 3-component data set *Cain et al.* [2003] inverted for a spherical harmonic degree and order 90 model of the Martian magnetic field. These data, covering the years 1998–2000, are from the AB, SPO and MO phases of the MGS mission. The data and their positions were given in an areodetic coordinate system, which were transformed to areocentric coordinates using equatorial and polar radii of 3396.9 km and 3374.9 km, respectively. Their (areodetic coordinate) altitudes range from 102 to 426 km. The higher-altitude data have almost uniform coverage, but the lower-altitude data have significant gaps in coverage, due to the positions of the orbits during the aerobraking phases. The full data set consisted of 3-component measurements at 111,274 points, i.e., 333,822 data.

[15] Maps of the r, θ and ϕ magnetic field components are shown in Figure 1. Data acquired above 160 km are shown in colour, and the horizontal gradient of data at lower altitudes is superimposed in shaded relief. These data show the by now familiar high amplitudes of the Martian magnetic field (exceeding 1200 nT in places), compared to the crustal anomaly field deduced for Earth, mainly confined to the area to the south of the dichotomy.

[16] *Cain et al.* [2003] allocated data to one of five classes depending on the mission phase, local time, and altitude range at which they were acquired. They deduced a standard deviation for each component in each class from a Gaussian fit to the residuals, which we used to define weights for inversion. These are summarized in Table 1. The extent of external field contamination is reflected by the amount the mean (not shown in Table 1) differs from zero and the size of the standard deviation. As expected, this is more serious in the horizontal field components. Applying the method described here to a preliminary MGS data set (with about half the number of data points), we found little difference between models calculated from only radial component data and when using all three components. However, the misfit to the data for the latter model was significantly higher. This also suggests that the horizontal components have larger uncertainties.

4. Results

[17] With such a large data set, we retained only the largest 0.21%, or 239×10^6, of the Gram matrix elements, and investigate a range of damping parameters; statistics of some solutions are given in Table 2. The threshold corresponding to this cut-off is 0.25, compared to a maximum element size of 129, i.e., elements were considered numerically negligible if they were less than 0.2% of the largest value. We have made extensive tests of the effect of varying the number of elements retained by inverting smaller data sets, including a terrestrial data set synthesized

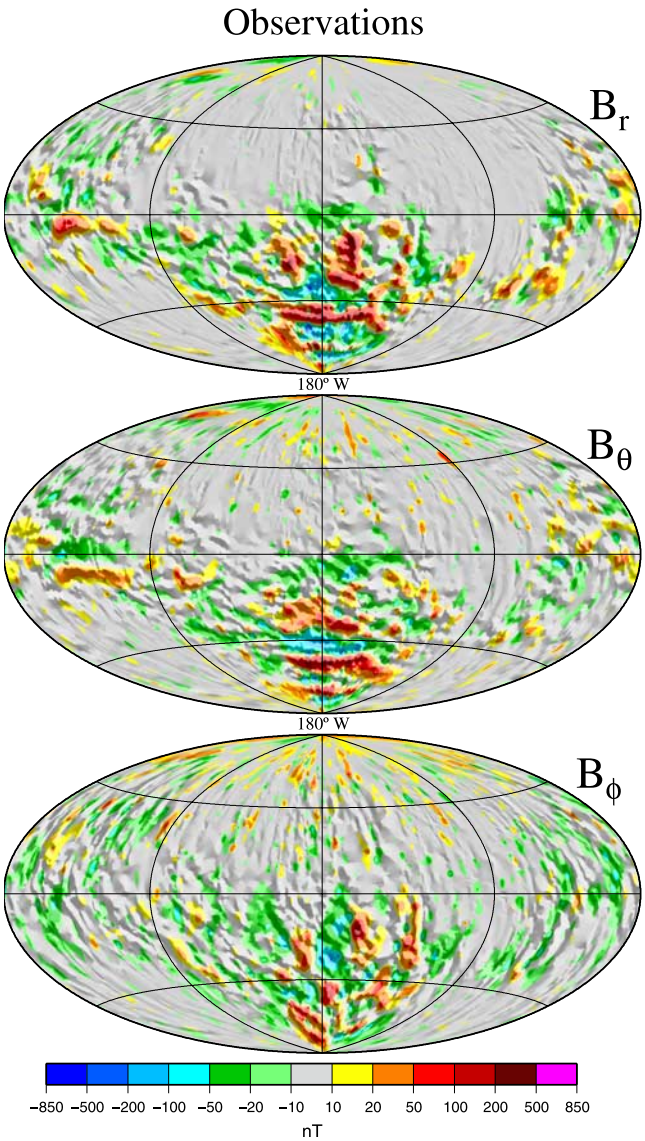

Figure 1. Observations which serve as input to the model. From top to bottom are shown B_r, B_θ, and B_ϕ. If the observations were acquired above 160 km altitude, they are shown in color; if below, they are shown as the horizontal gradient in shaded relief, illuminated from the north and west. The high-altitude data are binned into two degree bins, the low-altitude data are binned into one degree bins, and the median is plotted. Global Hammer projections are centered on the 180° meridian.

from *Maus et al.*'s [2002] spherical harmonic model of the scalar anomaly field determined by CHAMP [*Whaler*, 2003], the vertically downward component of a preliminary MGS data set [*Whaler and Purucker*, 2003], and the North and vertically downward components of a data set synthesized from the *Cain et al.* [2003] spherical harmonic model to degree and order 90, each of which contained about 50,000 data. In those cases, we were able to retain a higher percentage of the matrix elements, and found that changing the threshold below which elements were deemed numerically insignificant had only a small effect on the solution. We have also compared regional models produced using depleted basis or equivalent dipole methods with the appropriate areas of global terrestrial magnetization models deduced with the method outlined here using CG and found good agreement [*Whaler et al.*, 1996; *Whaler*, 2003]. We obtained a solution from the full *Cain et al.* [2003] data set by retaining just 0.07% (82×10^6) elements of the Gram matrix. The statistics of this model (see Table 2) are very similar to its counterpart with the same damping parameter when almost three times as many elements are retained, and plots of the magnetization components in the two cases are virtually indistinguishable. We conclude that the solution appears to be robust to a change in Gram matrix assumed sparseness, even when it is calculated from such a small fraction of matrix elements.

Table 1. Summary of the Weights in nT Applied to the Different Data Types[a]

Class	σ_r	σ_θ	σ_ϕ
AB1	6.5	9.5	9.9
AB2 (night)	6.7	7.1	6.2
AB2 (day)	10.3	13.5	13.0
SPO	6.4	10.5	11.4
MPO	5.9	5.3	6.8

[a]After *Cain et al.* [2003].

[18] For all but the smallest values of the damping parameter, and with preconditioning, the CG algorithm converged quickly, the number of iterations decreasing with increasing damping parameter. We defined convergence through a tolerance parameter measuring failure to satisfy equation (4) exactly, and required

$$\| \mathbf{d} - (\mathbf{\Gamma} + \lambda \mathbf{I})\boldsymbol{\alpha} \| < 10^{-10} \tag{7}$$

where $\|.\|$ denotes the two-norm length (recall that the diagonal elements of $\mathbf{\Gamma} + \lambda\mathbf{I}$ are unity after preconditioning). In one instance, we continued to run the CG algorithm once a tolerance of 10^{-10} was reached, since some studies have reported a gradual change to the solution (and associated misfit) as iteration continues. However, our solutions are stable if they achieve the specified tolerance; with further iterations, the tolerance quickly reached zero to machine precision without changing the solution. For very lightly damped solutions, convergence was not achieved by the maximum number of iterations specified (10,000). In these cases, although the tolerance parameter changed from iteration to iteration, there was no downward trend. We compared the sum of squares of residuals calculated from predictions of the data by the model against the algebraic

Table 2. Statistics Summarizing Some Inversions[a]

Threshold	Retained	λ	Iterations	Misfit	$\bar{M}$
0.25	0.21	50	550	2.4	0.77
0.25	0.21	100	75	2.3	0.93
0.25	0.21	10^3	15	4.3	0.31
0.25	0.21	10^4	7	5.5	0.05
0.6	0.07	10^4	7	5.5	0.04

[a]Threshold is the value below which Gram matrix elements are considered negligibly small, Retained indicates the percentage of Gram matrix elements retained with this threshold, λ is the damping parameter, Iterations indicates the number of CG iterations to achieve convergence, Misfit is the (weighted) misfit, and $\bar{M}$ is the mean crustal magnetization in A/m. Our preferred solution is the second one, with a mean crustal magnetization of 0.93 A/m.

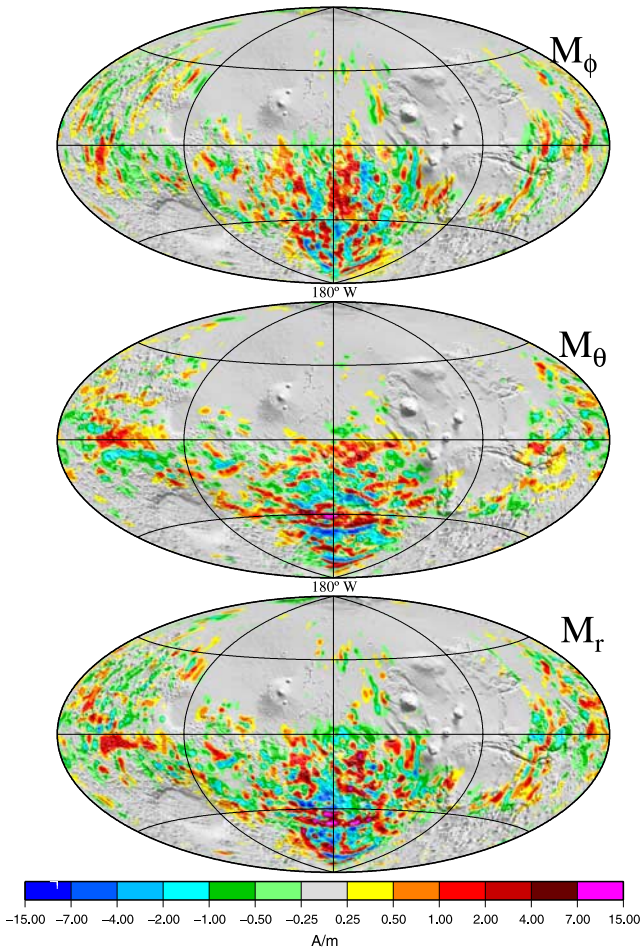

Figure 2. Magnetization model showing the three orthogonal components, M_r, M_θ, and M_ϕ. Each map is shown centered on the 180° meridian as a global Hammer projection.

expression for the sum of squares of residuals $\lambda^2\alpha^T\alpha$ [*Shure et al.*, 1982] obtained directly from the solution. The two values started to diverge for very light damping, which we took as further indication of lack of convergence. All models for which statistics are given in Table 2 are convergent.

[19] Figures 2 and 3 present **M** (calculated from (6)) at the Martian surface for our preferred solution ($\lambda = 100$ in Table 2); the extremal values (±20 A/m) are considerably higher than the crustal average (0.9 A/m), or even the average over the Martian surface (1.3 A/m). This reflects both the nonuniform distribution of magnetization, with much smaller values over most of the northern hemisphere, and the decrease in magnetization with depth through the magnetized layer. Large portions of the crust have magnetizations higher than values considered typical of the terrestrial crust, and exceeding *Parker*'s [2003] minimum value of about 7 A/m (interpolating his Figure 4 to a 40 km thick layer). A more heavily damped solution ($\lambda = 10^3$ in Table 2) shows a very similar pattern of magnetizations but a much lower amplitude (crustal average 0.3 A/m; maximum at the surface 5 A/m) which does not satisfy the Parker bound. Comparing Figures 2 and 1, we see that magnetization amplitudes are large where the magnetic field amplitude measured at satellite altitude is high, and vice versa; minimum norm solutions do not put structure where the data do not require it.

[20] The distribution of residuals for the model with $\lambda = 100$ is shown in Figure 4, in the same form as the original data in Figure 1. The significant variance reduction is immediately obvious (note the change in scale), with the largest residuals where the original data amplitudes were highest. The misfit for the three components is almost identical (25, 26 and 24 nT for the r, θ and ϕ components, respectively). Much of the short wavelength structure in the low-altitude data has been modeled.

[21] The weighted misfits given in Table 2 are all greater than unity, almost certainly indicating external field con-

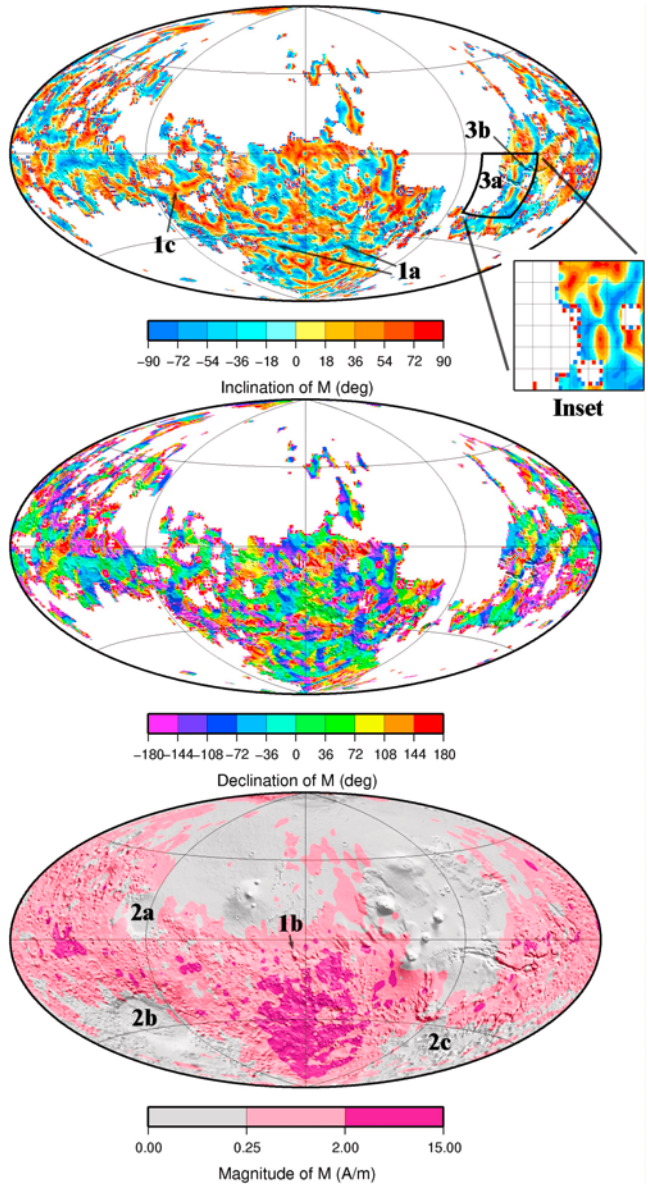

Figure 3. Magnetization model showing the magnitude of the magnetization, and the declination and inclination where the magnetization strength is sufficient for their definition. Each map is shown centered on the 180° meridian as a global Hammer projection. Labels are keyed to Table 4.

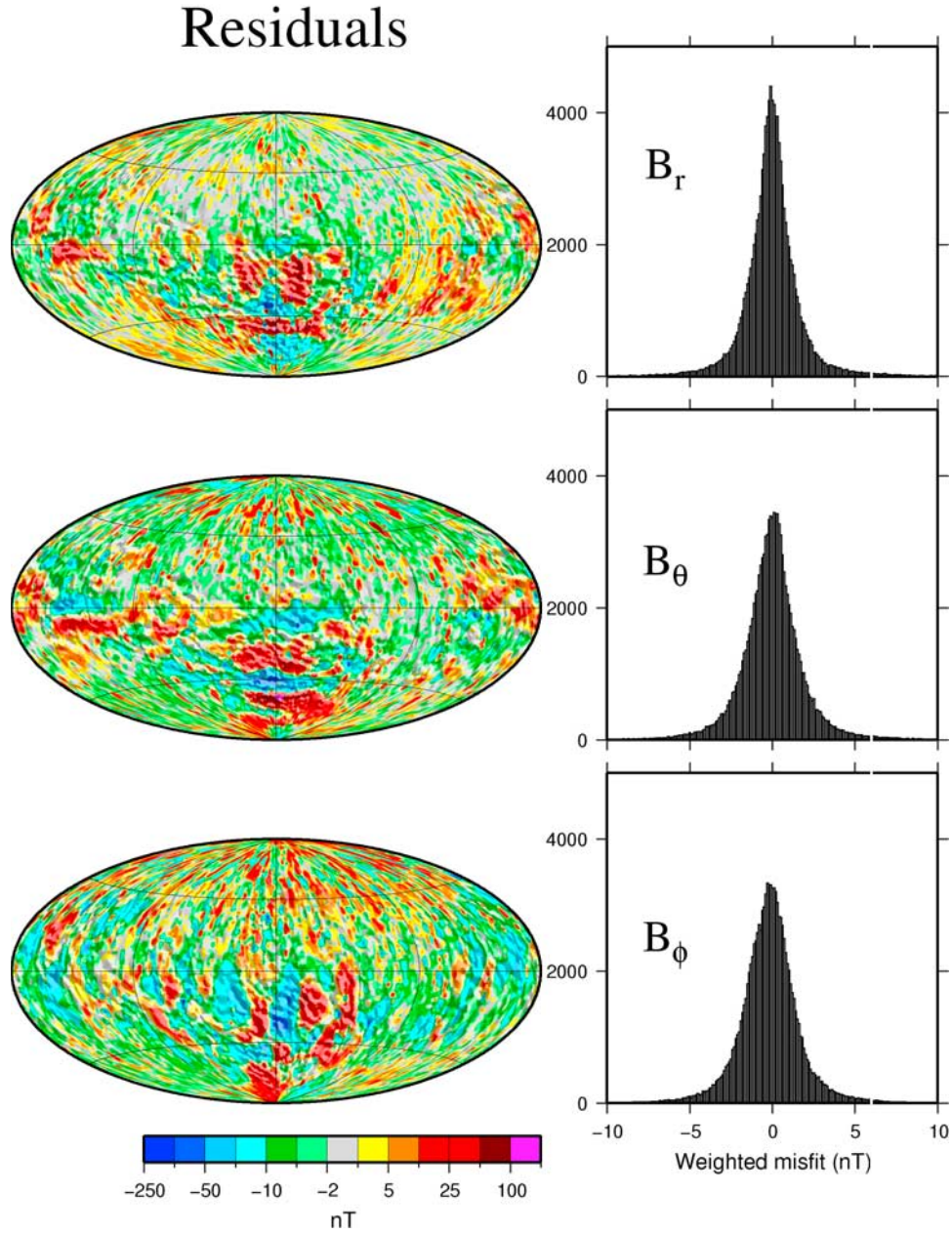

Figure 4. (left) Residuals and (right) weighted misfit. From top to bottom are shown B_r, B_θ, and B_ϕ. If the observations were acquired above 160 km altitude, their residuals are shown in color; if below, they are shown as the horizontal gradient in shaded relief, illuminated from the north and west. The high-altitude data are binned into two degree bins, the low-altitude data are binned into one degree bins, and the median is plotted. The contour levels at which the colors change is symmetric about 0 nT. Global Hammer projections are centered on the 180° meridian. The tails of the weighted misfits for B_r extend to ±65 nT; those for the other two components are smaller.

tamination of the data. We were unable to produce convergent solutions with smaller misfits. The weighted misfit to each component in each data class for the solution obtained with $\lambda = 100$ is given in Table 3. This shows that, despite using the standard deviations determined by *Cain et al.* [2003] from their spherical harmonic model fit, we are not fitting each weighted data type equally. The radial component data have the largest overall misfits, suggesting that external field contamination has been better compensated for in the horizontal components than in the radial component. The fit to the AB2 data is worse than average, and to the MPO data better than average, indicating that the standard deviations of the former are underestimated. The relative goodness-of-fit between the different data types also depends on the damping parameter. For instance, the average weighted misfit to the AB2 dayside data jumps

Table 3. Normalized RMS Misfits by Component and Data Type for the Model With $\lambda = 100$

Class	rms_r	rms_θ	rms_ϕ	rms
AB1	1.7	1.7	1.9	1.8
AB2 (night)	2.8	2.7	2.4	2.6
AB2 (day)	3.4	2.7	2.5	2.9
SPO	1.6	1.9	1.6	1.7
MPO	1.0	1.1	1.1	1.1
Overall	2.6	2.3	2.1	2.3

from 2.6 to 8.0, but that to the MPO data changes from 1.1 to only 1.2, when the damping parameter is increased from 100 to 10^3. Also, for our preferred model, the weighted misfit to the AB2 dayside data is larger than that to the AB2 nightside data, but the weighted nightside data are fit worse than the dayside data for larger damping parameters. A histogram of the weighted residuals to each component for the model with $\lambda = 100$ is also shown in Figure 4. They are more strongly peaked and have longer tails than a Gaussian distribution, probably reflecting the differences between the fits to the various data types. As they follow a Laplacian more closely than a Gaussian distribution, one-norm minimization would be a more appropriate inversion method [*Walker and Jackson*, 2000].

[22] The RMS magnetization and, even more spectacularly, the maximum and minimum magnetizations at the Martian surface, decrease rapidly as damping increases. We do not know how well we should expect to fit the data, since the level of external field contamination (probably the main source of error) is unknown, and this is not a zero mean, Gaussian noise source. A variation in the misfit of just over 2 (from 2.3 to 5.5) alters the RMS magnetization by a factor of about 20. This, combined with the inherent nonuniqueness of magnetization modeling, means our models do not constrain magnetization amplitudes in the Martian crust, nor therefore the likely magnetic carriers. However, the pattern of magnetizations is robust to changes in the damping parameter over a large range of values (at the very smallest values, the solution is dominated by more variable small-scale structure, presumably as the model tries to fit noise in the data). Thus angles defined from the magnetization models are robust. Figure 3 plots the inclination and declination of magnetization for our preferred model in areas where its strength is sufficiently large for these angles to be well defined. The pattern is broadly similar to that deduced from a preliminary data set [*Whaler and Purucker*, 2003], but with more structure reflecting the larger data set from which it was derived.

[23] Our magnetization solutions are available at http://planetary-mag.net/jgr_mars_whaler.

5. Discussion

[24] Our preferred model (Figure 2) is broadly similar to the preliminary model presented by *Whaler and Purucker* [2003]. However, the latter showed patches of high magnetization strength near the North Pole which were not reflected in plots of the input data. Since we were suspicious that they were caused by algebraic expressions blowing up near the poles, we rotated the data through 90° prior to inversion, such that points originally at the North Pole were treated as though they were on the equator. The resulting magnetization maps were identical to the originals rotated through the same angle. We now suspect instead that the high magnetizations were caused by a few relatively high amplitude data in high northern latitudes, possibly affected by external field contamination, that do not show up in maps of regularly gridded data.

[25] In Table 4 we propose a summary magnetic chronology for Mars, based partly on the magnetization models presented here. After the Martian dynamo began operation, a number of events were responsible for magnetic signatures seen in the MGS data. Within 0.5 billion years, the dynamo had ceased operation [*Acuña et al.*, 2001].

Table 4. A Chronology of Events With a Magnetic Signature

Code	Event	Location	Reference
	Initiation of Martian Dynamo		
	Overturn of primordial magma ocean(s), enhanced core heat flux and magnetic field generation, cooling of hot near-surface cumulates to produce an early magnetic crust	planetwide	*Elkins-Tanton et al.* [2003]
	Magnetic Field Creation Events		
1a	Development of lineated magnetic features associated with crustal recycling	Terra Sirenum and Cimmeria	*Connerney et al.* [1999]
1b	Development of magnetic features associated with volcanism and plutonism	proto-Apollinarsis Patera	*Langlais and Purucker* [2003]
1c	Development of magnetic features associated with volcanism and tectonism	proto-Tyrrhena Patera	*Whaler and Purucker* [2003]
	Martian Dynamo Disappears		
	Magnetic Field Destruction Events		
2a	Impact	Isidis	*Acuña et al.* [1999]
2b	Impact	Hellas	*Acuña et al.* [1999]
2c	Impact	Argyre	*Acuña et al.* [1999]
	Later Tectonic Events		
3a	Extensional tectonics	Valles Marineris	*Purucker et al.* [2000], this study
3b	Extensional tectonics?	Ganges Chasma	*Purucker et al.* [2000], this study

Subsequently, heating and impacts have demagnetized patches of the crust, and tectonic activity has stretched and offset magnetization structures; these magnetic destructive and tectonic events may have been contemporaneous.

[26] The new magnetization model clearly shows that tectonism in the Valles Marineris region has a magnetic signature, first recognized by *Purucker et al.* [2000]. The signature is most pronounced in the inclination of the magnetization vector (inset in Figure 3), where a throughgoing, N-S trending, positive magnetization feature is disrupted at Valles Marineris (3a). Although the feature is disrupted, there is no evidence for offset, and hence an extensional origin is preferred, consistent with other tectonic indicators [*Schultz and Lin*, 2001]. The situation is less clear to the north at Ganges Chasma (3b), where *Purucker et al.* [2000] commented on the apparent offset or truncation of a positive B_r feature. While there is a bend in this feature, there is no convincing evidence that it is either truncated or offset.

[27] Large volcanoes of the Tharsis region show an almost complete absence of magnetization, ascribed to thermal demagnetization [*Johnson and Phillips*, 2005]. In contrast, volcanism south of the dichotomy boundary is associated with magnetized terranes in at least two instances, Apollinaris Patera [*Langlais and Purucker*, 2003] and Tyrrhena Patera [*Whaler and Purucker*, 2003]. In both cases the volcanic centers also have associated gravity anomalies. Apollinaris Patera, located at the boundary between the northern plains and the southern highlands, has a 5 km high volcanic edifice centered on a 200 km wide dome, and the caldera is some 75 km wide. Located at (9°S, 174°E) the exposed volcano is of Lower Hesperian to Lower Amazonian age [*Robinson et al.*, 1993]. A 215 mGal gravity anomaly is coincident with the volcanic edifice [*Lemoine et al.*, 2001], and the associated magnetic feature is some 300 km in diameter and indicative of a high inclination magnetization [*Langlais and Purucker*, 2003]. Tyrrhena Patera, in contrast, is an areally extensive, degraded volcanic center [*Greeley and Crown*, 1990] northeast of Hellas that is largely Hesperian in age. There is a 145 mGal gravity anomaly associated with it, recently interpreted [*Kiefer*, 2003] as a high density magma chamber 275–300 km wide and at least 2.9 km thick. The associated magnetic feature is highly unusual, and consists of three ''arms'' of steep inclination originating from the caldera region at (21°S, 106°E), but extending significantly beyond the volcanic edifice. This feature was interpreted as a triple junction formed in a reversing magnetic field [*Whaler and Purucker*, 2003]. Marked as feature 1c in Figure 3, it can be seen in more detail in Figure 3 of *Whaler and Purucker* [2003]. It might alternatively be associated with fracturing, and subsequent intrusions, occurring during the development of a proto-Tyrrhena Patera volcanic system in a reversing magnetic field.

[28] Another interesting feature (1a in Figure 3) is the linear (in the equal azimuth map projection used) ''channel'' of approximately constant 0° declination and −90° inclination magnetization running between 145° and 214° W in the Cimmeria region, surrounded by regions of normal (i.e., similar to that seen elsewhere in the southern hemisphere) variability. The sharp southern edge is the boundary between positive (to the north) and negative (to the south) radial magnetic field, modeled here as a switch from −90° to +90° magnetization inclination. Thus it is consistent with generation by a process analogous to the formation of terrestrial seafloor magnetic stripes [*Connerney et al.*, 1999], or dike intrusion [*Nimmo*, 2000] over a period during which the magnetic field was steady, and different from that when the surrounding crust was magnetized. Alternatively, as the locus of the boundary is a great circle arc, the inclination reversal across it is reminiscent of the pattern associated with a terrestrial transform fault.

[29] Forward models of 10 ''isolated'' magnetic features, primarily north of the dichotomy, have been developed by *Arkani-Hamed* [2001b]. He assumed they were caused by elliptical prisms 10 km thick, and determined the prisms' magnetization strengths and directions, and hence paleopole positions. Since the two modeling methods are markedly different in approach, it is perhaps not surprising that our (preferred solution) paleopoles for these same features are close (separated by less than 30°) to his for only half of them, although their average separation is only 35°. The result does not depend on the depth at which our magnetizations are calculated, and is only mildly sensitive to damping parameter. The forward models of *Arkani-Hamed* [2001b] and our inverse models provide evidence for reversals. Many paleopoles are displaced from the current rotation pole, which may suggest plate tectonic movement (such that the site was originally at a rotation pole), or a dynamo field that was either predominantly nondipolar or dipolar but not aligned along the rotation axis. Martian polar wander has previously been identified by *Arkani-Hamed and Boutin* [2004] and *Hood and Zakharian* [2001].

[30] *Langlais et al.* [2004] have inverted Martian magnetic data for equivalent dipole models of magnetization based on the CG method of *Purucker et al.* [1996]. Unlike the terrestrial case, when it is reasonable to assume the dipoles are aligned with the current (inducing) main magnetic field, they solved for both magnitudes and directions. Despite the differences in both the data sets and modeling algorithms, and the ways in which a preferred model is chosen from the infinity of possible solutions, there is close similarity between ours and their preferred model, in which the dipoles were embedded in a 40 km thick layer. This can be quantified by cross-correlating the two models (evaluating ours at 20 km depth, though again the result is insensitive to the depth specified), giving correlation coefficients of 0.92, 0.94 and 0.88 for the r, θ and ϕ magnetization components, respectively. All three coefficients are highly significant, i.e., the probability of obtaining these values from uncorrelated models is negligibly small. Further statistical tests depend on the models having Gaussian distributed magnetizations [*Press et al.*, 1992], which is clearly not the case. The correlation coefficients are mildly sensitive to the damping parameter chosen, dropping a little as the damping parameter increases. This presumably reflects correlation between small-scale structure in our less damped solutions, controlled largely by the lower altitude AB phase data that are preferentially better fit, that is also present in *Langlais et al.*'s [2004] preferred model. However, the conclusion of a statistically significant correlation between the models of the two methods is robust, regardless of damping parameter. We also undertook a linear regression of one model onto the other; whereas a correlation analysis quantifies the degree to which the

patterns are similar, regression additionally identifies any differences between mean value (indicated by the intercept) and amplitude (indicated by the slope). All three intercepts were negligibly small, but the slopes were 0.77, 0.72 and 0.62 for the r, θ and ϕ components, respectively. Thus, besides having an overall slightly lower amplitude, our preferred model puts proportionally more power in the r component (and less in the ϕ component) than *Langlais et al.*'s [2004].

[31] *Arkani-Hamed* [2002a] takes a different approach to constructing a magnetization map, and assumes that the Martian magnetic field over its entire history can be described by a dipole field with a pole NE of Olympus Mons, and that this pattern was not subsequently disrupted by tectonic activity. Although a dipolar magnetic field would be a reasonable assumption on earth, the application of this technique to terrestrial magnetic field observations would yield spurious results because of both plate tectonics and polar wander. Similar considerations [*Connerney et al.*, 1999] may limit the applicability of this technique at Mars. The pole was determined as a mean of several paleomagnetic poles calculated from ''isolated'' features. A transformation [*Arkani-Hamed and Dyment*, 1996] is then applied to convert the degree 50 spherical harmonic model of *Arkani-Hamed* [2001a] into a map of magnetization. Magnetization contrasts as high as 35 A/m are a consequence of the selection of the particular paleopole, which results in the highly magnetic Cimmeria region being located on the paleoequator. The magnetization solution in this region is thus dominated by large horizontal magnetizations. Recognizable radial magnetizations of alternating polarity corresponding to spherical harmonic degree 50 can be seen north of Cimmeria, and north of the present Martian equator, where measured magnetic fields are weak. These are interpreted here as truncation features.

6. Conclusions

[32] The methodology presented here, based on previous work by *Parker et al.* [1987], *Jackson* [1990], and *Whaler and Langel* [1996], has been used to produce magnetization models for the Martian crust from the MGS data set compiled by *Cain et al.* [2003]. Magnetization was expressed as a continuous function of position within the magnetized crust, assumed 40 km thick, and no assumptions were made about its direction. We obtained a linear system of equations of dimension the number of data, which is impractical to solve by direct means. By taking advantage of the numerical sparseness of the linear system, we were able to use the iterative CG algorithm on a multiple processor system to invert the data. The majority of the computational effort went into calculating the sparse matrix, and this parallelizes efficiently. The resulting magnetizations are similar to those obtained from previous modeling strategies, both forward and inverse, despite their inherent nonuniqueness. In our case, the unique model minimizing the RMS magnetization amplitude for a given fit to the data was chosen. The pattern of magnetizations remains remarkably similar over a wide range of fits, although the magnetization strength varies considerably.

[33] Our magnetization models can be used to predict the magnetic field at any point outside the planet; e.g., they can be used to reduce satellite data to a common altitude. The results of this agree favorably with other leveling methods, such as equivalent dipole magnetization and spherical harmonic modeling. However, different types of model with the same RMS misfit fit individual data points differently, and this difference is also reflected in field predictions. Figure 5 compares the magnetic field power spectra from spherical harmonic analysis (SHA) by *Cain et al.* [2003], *Connerney et al.* [2001], and *Arkani-Hamed* [2004], and of the predictions of the magnetization models of *Langlais et al.* [2004] and our preferred model, all evaluated at Mars' surface. SHA power spectra continue to rise when plotted at the surface, whereas those derived from magnetization models reach a maximum at about harmonic degree 50, with only a little less power at wavelengths well resolved by the data. Divergent power spectra imply nonphysical models (e.g., negative depths to sources) and we thus recommend the use of magnetization models over SHA for downward continuation. Conversely, we recommend *Cain et al.* [2003] over our magnetization model for upward continuation. The lower magnetization amplitude of our preferred model compared to *Langlais et al.*'s [2004] is reflected in its predicted magnetic field power spectrum. Figure 5 also shows the degree correlation of the predictions of our magnetization model with other models, demonstrating the excellent agreement to approximately degree 50.

[34] From our models, we identify features similar to magnetization patterns associated with the results of tectonic activity and magnetic reversals on Earth. These include magnetic stripes of alternating polarity, the coincidence of magnetic and gravity anomalies over volcanic centers, truncations in otherwise linear magnetization features, and polar wander. Large sections of the surface, particularly north of the dichotomy, are essentially unmagnetized, reflecting activity after the Martian dynamo had switched off. We have developed a chronology of events corresponding to the magnetization features of our model, aiding structural and tectonic interpretation.

[35] In future work, we intend to investigate further the predictions and interpretation of our model, including the magnetization correlation length, and whether it varies across the dichotomy. Continuing MGS operation may improve the data set to the extent that further models are justified, in which case we would hope to strengthen the conclusions developed here. Although we are unable to produce robust estimates of Martian magnetization strength, three factors point to it being significantly higher than on Earth. Firstly, a comparison between the size of terrestrial and Martian magnetic anomalies at satellite altitude. Secondly, the original magnetizations will have been decaying viscously and by chemical alteration over the $\sim$4 billion years since acquisition. As they are based purely on satellite data, our models do not contain wavelengths shorter than around 200 km. On Earth, aeromagnetic, marine and ground-based measurements indicate that short wavelength features typically have much higher amplitudes than those of intermediate wavelength features inferred from satellite data when compared at the same altitude. If the same is true for Mars, again higher magnetizations are suggested.

[36] We conclude that the magnetic mineralogy and/or strength of the Martian dynamo field must have been very

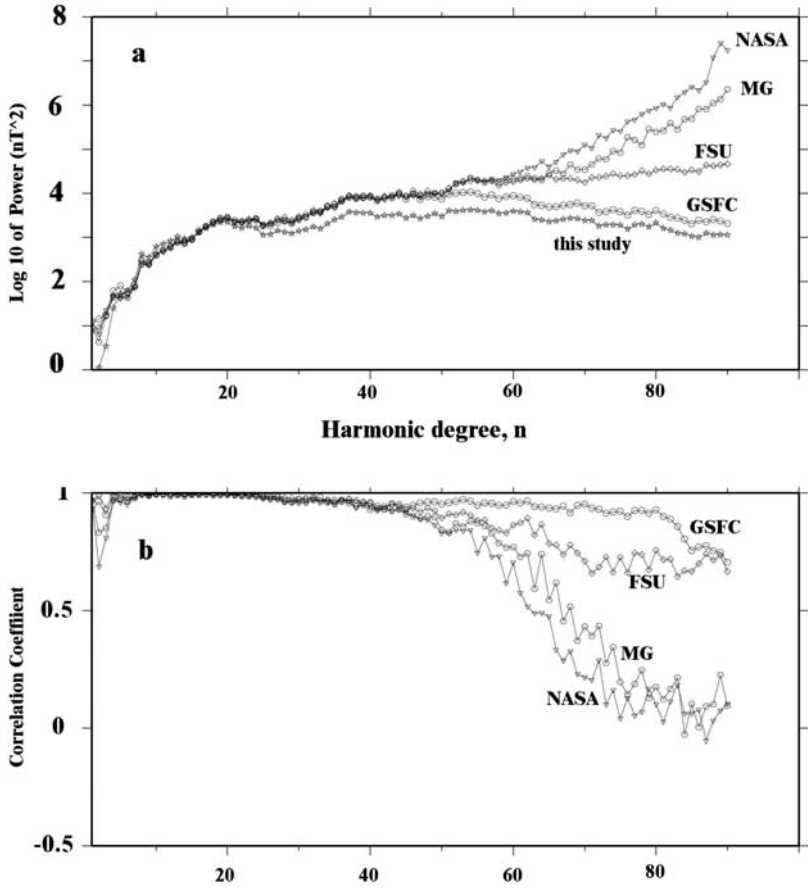

Figure 5. (a) Comparison of the Lowes-Mauersberger power spectra at the surface of Mars from this and other models. The spectrum is the mean square amplitude of the magnetic field over a sphere produced by harmonics of degree *n*. NASA is the model of *Connerney et al.* [2001], FSU is the model of *Cain et al.* [2003], GSFC is the model of *Langlais et al.* [2004], and MG is the model of *Arkani-Hamed* [2004]. (b) The degree correlation of this model compared with the other models.

different from that on Earth when magnetization was acquired, providing significant challenges to the mineral magnetic and planetary dynamo communities. Candidate magnetic carriers (requiring high magnetization and coercivity), either responsible for primary magnetization or that resulting from impacts, include haematite [e.g., *Christensen et al.*, 2001; *Dunlop and Kletetschka*, 2001; *Hynek et al.*, 2002], pyrrhotite [e.g., *Rochette et al.*, 2001, 2003] and lamellae of hemo-ilmenite [*McEnroe et al.*, 2004a, 2004b]. Haematite has recently been identified in Martian rocks by surface rovers [*Christensen et al.*, 2004; *Klingelhöfer et al.*, 2004; *Rieder et al.*, 2004]. More energetic core convection early in Mars' history may have resulted in a higher field strength dynamo and consequent faster cooling, causing dynamo activity to cease at a relatively early stage. Determination of Mars' moment of inertia [*Yoder et al.*, 2003] indicates that it still has a partially fluid core, and hence that the areotherm became subadiabatic, rather than the core froze completely. Scenarios for core evolution are discussed by *Stevenson* [2001].

[37] **Acknowledgments.** All graphs and maps have been plotted using the Generic Mapping Tools software [*Wessel and Smith*, 1991]. Part of this work was performed while KAW was on leave from the University of Edinburgh as a Goddard Visiting Fellow in the Earth Sciences at the NASA/Goddard Space Flight Center, Greenbelt, Maryland. The Goddard Visiting Fellowship is a program of the Goddard Earth Sciences and Technology Center, University of Maryland, Baltimore County. Most of the inversions were performed on the University of Edinburgh Parallel Computing Centre (EPCC) sunfire cluster. Code parallelization was undertaken by undergraduate students Magnus Hagdorn, Adam Carter and Josephine Beech-Brandt, the last two as participants in the EPCC Summer Scholarship Programme. Undergraduate student Tim Seher also contributed to program development. MEP was supported by MDAP Contract NASW-02025. We would like to thank Lon Hood and an anonymous reviewer for helpful suggestions.

References

Acuña, M. H., et al. (1999), Global distribution of crustal magnetization discovered by the Mars Global Surveyor MAG/ER experiment, *Science*, *284*, 790–793.

Acuña, M. H., et al. (2001), Magnetic field of Mars: summary of results from the AeroBraking and mapping orbits, *J. Geophys. Res.*, *106*, 23,403–23,417.

Albee, A. L., R. E. Arvidson, F. Palluconi, and T. Thorpe (2001), Overview of the Mars Global Surveyor Mission, *J. Geophys. Res.*, *106*, 23,291–23,316.

Arkani-Hamed, J. (2001a), A 50-degree spherical harmonic model of the magnetic field of Mars, *J. Geophys. Res.*, *106*, 23,197–23,208.

Arkani-Hamed, J. (2001b), Paleomagnetic pole positions and pole reversals of Mars, *Geophys. Res. Lett.*, *28*, 3409–3412.

Arkani-Hamed, J. (2002a), Magnetization of the Martian crust, *J. Geophys. Res.*, *107*(E5), 5032, doi:10.1029/2001JE001496.

Arkani-Hamed, J. (2002b), An improved 50-degree spherical harmonic model of the magnetic field of Mars derived from both high-altitude and low-altitude data, *J. Geophys. Res.*, *107*(E10), 5083, doi:10.1029/2001JE001835.

Arkani-Hamed, J. (2004), A coherent model of the crustal magnetic field of Mars, *J. Geophys. Res.*, *109*, E09005, doi:10.1029/2004JE002265.

Arkani-Hamed, J., and D. Boutin (2004), Paleomagnetic poles of Mars: Revisited, *J. Geophys. Res.*, *109*, E03011, doi:10.1029/2003JE002229.

Arkani-Hamed, J., and J. Dyment (1996), Magnetic potential and magnetization contrasts of Earth's lithosphere, *J. Geophys. Res.*, *101*, 11,401–11,425.

Cain, J. C., B. B. Ferguson, and D. Mozzoni (2003), An $n = 90$ internal potential function of the Martian crustal magnetic field, *J. Geophys. Res.*, *108*(E2), 5008, doi:10.1029/2000JE001487.

Christensen, P. R., R. V. Morris, M. D. Lane, J. L. Bandfield, and M. C. Malin (2001), Global mapping of Martian hematite mineral deposits: Remnants of water-driven processes on early Mars, *J. Geophys. Res.*, *106*, 23,873–23,886.

Christensen, P. R., et al. (2004), Mineralogy at Meridiani Planum from the Mini-TES experiment on the Opportunity Rover, *Science*, *306*, 1733–1739.

Connerney, J. E. P., M. H. Acuña, P. J. Wasilewski, N. F. Ness, H. Rème, C. Mazelle, D. Vignes, R. P. Lin, D. Mitchell, and P. Cloutier (1999), Magnetic lineations in the ancient crust of Mars, *Science*, *284*, 794–798.

Connerney, J. E. P., M. H. Acuña, P. J. Wasilewski, G. Kletetschka, N. F. Ness, H. Rème, R. P. Lin, and D. L. Mitchell (2001), The global magnetic field of Mars and implications for crustal evolution, *Geophys. Res. Lett.*, *28*, 4015–4018.

Dunlop, D. J., and G. Kletetschka (2001), Multidomain hematite: A source for planetary magnetic anomalies?, *Geophys. Res. Lett.*, *28*, 3345–3348.

Elkins-Tanton, L. T., E. M. Parmentier, and P. C. Hess (2003), Magma ocean fractional crystallization and cumulate overturn in terrestrial planets: Implications for Mars, *Meteorit. Planet. Sci.*, *38*(12), 1753–1771.

Greeley, R., and D. A. Crown (1990), Volcanic geology of Tyrrhena Patera, Mars, *J. Geophys. Res.*, *95*(B5), 7133–7149.

Hood, L. L., and A. Zakharian (2001), Mapping and modeling of magnetic anomalies in the northern polar region of Mars, *J. Geophys. Res.*, *106*(E7), 14,601–14,620.

Hynek, B. M., R. E. Arvidson, and R. J. Phillips (2002), Geologic setting and origin of Terra Meridiani hematite deposit on Mars, *J. Geophys. Res.*, *107*(E10), 5088, doi:10.1029/2002JE001891.

Jackson, A. (1990), Accounting for crustal magnetization in models of the core magnetic field, *Geophys. J. Int.*, *103*, 657–673.

Johnson, C. L., and R. J. Phillips (2005), Evolution of the Tharsis region of Mars: Insights from magnetic field observations, *Earth Planet. Sci. Lett.*, *230*, 241–254.

Kiefer, W. S. (2003), Gravity evidence for extinct magma chambers on Mars: Tyrrhena Patera and Hadriaca Patera, *Proc. Lunar Planet. Sci. Conf., 34th*, Abstract 1234.

Klingelhöfer, G., et al. (2004), Jarosite and hematite at Meridiani Planum from Opportunity's Mössbauer spectrometer, *Science*, *306*, 1740–1745.

Langlais, B., and M. Purucker (2003), A polar magnetic paleopole on Mars?, *Eos Trans. AGU*, *84*(46), Fall Meet. Suppl., Abstract GP21D-08.

Langlais, B., M. E. Purucker, and M. Mandea (2004), Crustal magnetic field of Mars, *J. Geophys. Res.*, *109*, E02008, doi:10.1029/2003JE002048.

Lemoine, F. G., D. E. Smith, D. D. Rowlands, M. T. Zuber, G. A. Neumann, D. S. Chinn, and D. E. Pavlis (2001), An improved solution of the gravity field of Mars (GMM-2B) from Mars Global Surveyor, *J. Geophys. Res.*, *106*, 23,359–23,376.

Maus, S., and V. Haak (2003), Magnetic field annihilators: Invisible magnetization at the magnetic equator, *Geophys. J. Int.*, *155*, 509–513.

Maus, S., M. Rother, R. Holme, H. Lühr, N. Olsen, and V. Haak (2002), First scalar magnetic anomaly map from CHAMP satellite data indicates weak lithospheric field, *Geophys. Res. Lett.*, *29*(14), 1702, doi:10.1029/2001GL013685.

McEnroe, S. A., J. R. Skilbrei, P. Robinson, F. Heidelbach, F. Langenhorst, and L. L. Brown (2004a), Magnetic anomalies, layered intrusions and Mars, *Geophys. Res. Lett.*, *31*, L19601, doi:10.1029/2004GL020640.

McEnroe, S. A., L. L. Brown, and P. Robinson (2004b), Earth analog for Martian magnetic anomalies: Remanence properties of hemo-ilmenite norites in the Bjerkreim-Sokndal intrusion, Rogaland, Norway, *J. Appl. Geophys.*, *56*, 195–212.

Neumann, G. A., M. T. Zuber, M. A. Wieczorek, P. J. McGovern, F. G. Lemoine, and D. E. Smith (2004), Crustal structure of Mars from gravity and topography, *J. Geophys. Res.*, *109*, E08002, doi:10.1029/2004JE002262.

Nimmo, F. (2000), Dike intrusion as a possible cause of linear Martian magnetic anomalies, *Geology*, *28*, 391–394.

Nimmo, F., and M. S. Gilmore (2001), Constraints on the depth of magnetized crust on Mars from impact craters, *J. Geophys. Res.*, *106*, 11,315–11,323.

Parker, R. L. (1994), *Geophysical Inverse Theory*, 386 pp., Princeton Univ. Press, Princeton, N. J.

Parker, R. L. (2003), Ideal bodies for Mars magnetics, *J. Geophys. Res.*, *108*(E1), 5006, doi:10.1029/2001JE001760.

Parker, R. L., and L. Shure (1982), Efficient modeling of the Earth's magnetic field with harmonic splines, *Geophys. Res. Lett.*, *9*, 812–815.

Parker, R. L., L. Shure, and J. A. Hildebrand (1987), The application of inverse theory to seamount magnetism, *Rev. Geophys.*, *25*, 17–40.

Press, W. H., S. A. Teukolsky, W. T. Vetterling, and B. P. Flannery (1992), *Numerical Recipes in C: The Art of Scientific Computing*, 2nd ed., pp. 71–89, Cambridge Univ. Press, New York.

Purucker, M. E., T. J. Sabaka, and R. A. Langel (1996), Conjugate gradient analysis: A new tool for studying satellite magnetic data sets, *Geophys. Res. Lett.*, *23*, 507–510.

Purucker, M. E., D. Ravat, H. Frey, C. Voorhies, T. Sabaka, and M. Acuña (2000), An altitude-normalized magnetic map of Mars and its interpretation, *Geophys. Res. Lett.*, *27*, 2449–2452.

Purucker, M., J. Connerney, M. Mandea, and G. Hulot (2003), A test for secular variation of the Martian magnetic field, paper presented at EGS-AGU-EUG Joint Assembly, abstract 7394, Nice, France, 6–11 April.

Ravat, D., K. A. Whaler, M. Pilkington, T. Sabaka, and M. Purucker (2002), Compatibility of high-altitude aeromagnetic and satellite-altitude magnetic anomalies over Canada, *Geophysics*, *67*, 546–554.

Rieder, R., et al. (2004), Chemistry of rocks and soils at Meridiani Planum from the alpha particle X-ray spectrometer, *Science*, *306*, 1746–1749.

Robinson, M. S., P. J. Mouginis-Mark, J. R. Zimbelman, S. S. C. Wu, K. K. Ablin, and A. E. Howington-Kraus (1993), Chronology eruption duration, and atmospheric contribution of the Martian volcano Apollinaris Patera, *Icarus*, *104*, 301–323.

Rochette, P., J. P. Lorand, G. Fillion, and V. Sautter (2001), Pyrrhotite and the remanent magnetization of SNC meteorites: A changing perspective on Martian magnetism, *Earth Planet. Sci. Lett.*, *190*, 1–12.

Rochette, P., G. Fillion, R. Ballou, F. Brunet, B. Oulladiaf, and L. Hood (2003), High pressure magnetic transition in monoclinic pyrrhotite (Fe7S8) and impact demagnetization on Mars, paper presented at EGS-AGU-EUG Joint Assembly, EAE03-A-01526, Nice, France, 6–11 April.

Runcorn, S. K. (1975), On the interpretations of lunar magnetism, *Phys. Earth Planet. Inter.*, *10*, 327–335.

Schultz, R. A., and J. Lin (2001), Three-dimensional normal faulting models of the Valles Marineris, Mars, and geodynamic implications, *J. Geophys. Res.*, *106*, 16,549–16,566.

Shure, L., R. L. Parker, and G. E. Backus (1982), Harmonic splines for geomagnetic modelling, *Phys. Earth Planet. Inter.*, *28*, 215–229.

Smith, D. E., et al. (2001), Mars Orbiter Laser Altimeter: Experiment summary after the first year of global mapping of Mars, *J. Geophys. Res.*, *106*, 23,689–23,722.

Stevenson, D. J. (2001), Mars' core and magnetism, *Nature*, *412*, 214–219.

Walker, M. R., and A. Jackson (2000), Robust modelling of the Earth's magnetic field, *Geophys. J. Int.*, *143*, 799–808.

Wessel, P., and W. H. F. Smith (1991), Free software helps map and display data, *Eos Trans. AGU*, *72*, 441–448.

Whaler, K. A. (2003), Crustal magnetisation deduced from CHAMP data, in *First CHAMP Mission Results for Gravity, Magnetics and Atmospheric Studies*, edited by C. H. Reigber, H. Lühr, and P. Schwinter, pp. 281–287, Springer, New York.

Whaler, K. A., and R. A. Langel (1996), Minimal crustal magnetizations from satellite data, *Phys. Earth Planet. Inter.*, *98*, 303–319.

Whaler, K. A., and M. E. Purucker (2003), Martian magnetization—Preliminary models, *Leading Edge*, *22*, 763–765.

Whaler, K. A., R. A. Langel, A. Jackson, and M. E. Purucker (1996), Non-uniqueness in magnetization: Crustal models from satellite magnetic data, *Eos Trans. AGU*, *77*(46), Fall Meet. Suppl., F172.

Yoder, C. F., A. S. Konopliv, D. N. Yuan, E. M. Standish, and W. M. Folkner (2003), Fluid core size of Mars from detection of the solar tide, *Science*, *300*, 299–303.

Zuber, M. T., et al. (2000), Internal structure and early thermal evolution of Mars from Mars Global Surveyor topography and gravity, *Science*, *287*, 1788–1793.

M. E. Purucker, Raytheon ITSS at Planetary Geodynamics Laboratory, NASA/GSFC, Greenbelt, MD 20771, USA. (purucker@geomag.gsfc.nasa.gov)

K. A. Whaler, Institute of Earth Science, School of GeoSciences, University of Edinburgh, West Mains Road, Edinburgh EH9 3JW, UK. (kathy.whaler@ed.ac.uk)